Biosensors and Bioelectronics: X 18 (2024) 100472

Contents lists available at ScienceDirect

Biosensors and Bioelectronics: X

journal homepage: www.journals.elsevier.com/biosensors-and-bioelectronics-x

Low-cost ultrasensitive flexible carbon fiber-based biosensor for the detection of SARS-CoV-2 in human saliva

Steffane Q. Nascimento [a], Rodrigo M. Iost [a], Thiago C. Oliveira [a], Rafael N. Colombo [a], Luana C.I. Faria [a], Thiago Bertaglia [a], Jéssica C. Pacheco [a], Mona N. Oliveira [b], Erika R. Manuli [c,d], Geovana M. Pereira [c], Ester C. Sabino [c,d], Frank N. Crespilho [a,*]

[a] São Carlos Institute of Chemistry, University of São Paulo (USP), São Carlos, SP, 13560-590, Brazil
[b] Biolinker Synthetic Biology EIRELI, São Paulo, Brazil
[c] Institute of Tropical Medicine of the Faculty of Medicine, University of São Paulo, Sao Paulo, Brazil
[d] University of São Caetano do Sul, São Paulo, Brazil

ARTICLE INFO

Keywords:
COVID-19
SARS-CoV-2
Ultrasensitive biosensor
Flexible carbon fiber
Human saliva

ABSTRACT

The ongoing COVID-19 pandemic continues to have a significant impact on our daily lives, necessitating the rapid development of early diagnostic tools to mitigate the emergence of severe acute respiratory syndrome coronavirus 2 (SARS-CoV-2) outbreaks. In this context, biosensor technology has emerged as a highly promising strategy to address the challenges of low sensitivity, specificity, and high cost associated with clinical diagnosis. In this study, we present a novel and cost-effective approach for the rapid detection of SARS-CoV-2 using miniaturized flexible carbon fiber (FCF) electrodes that are modified with immunoglobulin G (IgG). Our strategy take advantage of on the antigen-antibody interaction (IgG-SARS-CoV-2) and leverages the surface chemistry characteristics of FCF to achieve signal amplification. Under standard conditions, we achieved a remarkable detection limit of 0.16 pg mmL^{-1} for the SARS-CoV-2 RBD protein. Additionally, when analyzing human saliva samples, our biosensing approach demonstrated good agreement with RT-PCR results, specifically for patients who tested positive for SARS-CoV-2. The sensitivity, selectivity, and accuracy of our approach were approximately 93.3%.

1. Introduction

Coronaviruses (CoVs) are large, single-stranded RNA viruses that have caused fatal pneumonia in humans since the beginning of the 21st cen tury (Wiersinga et al., 2020). The severe acute respiratory syndrome coronavirus (SARS-CoV) (Zhong et al., 2003) and Middle East respiratory syndrome coronavirus (MERS-CoV) (Zaki et al., 2012) were the first two human pathogenic respiratory illnesses of major concern. In December 2019, the International Committee on Taxonomy of Viruses (ICTV) identified severe acute respiratory syndrome coronavirus 2 (SARS-CoV-2) (Gorbalenya et al., 2020). SARS-CoV-2, also known as coronavirus disease 2019 (COVID-19), belongs to the beta coronavirus family. It shares 79% and 50% genome sequence identity with SARS-CoV and MERS-CoV, respectively (Lu et al., 2020). By January 2023, the virus had spread worldwide, infecting more than 600 million people and resulting in 6.6 million deaths, according to the World Health Organization (Behura et al., 2023). The global economy and society are still in the process of recovering from the COVID-19 pandemic, largely due to the rapid spread and emergence of highly contagious variants such as Omicron (Dhama et al., 2023) and Delta (Gomari et al., 2023). In the recent scenario, developing new strategies for feasible detection remains a fundamental issue regards to a better quality of life (Ravi et al., 2020).

SARS-CoV-2 has diameters ranging from 60 nm to 140 nm, with distinctive protein spikes measuring 9 nm–12 nm (solar corona-like nanostructures) (Goldsmith et al., 2004). These spikes interact specifically with angiotensin-converting enzyme 2 (Hoffmann et al., 2020). The coronavirus spike glycoprotein serves as a crucial target for vaccine development and novel diagnostic strategies (Wrapp et al., 2020). Currently, various experimental approaches exist for detecting SARS-CoV-2, including the use of antigens, antibodies, and viral particles (Mao et al., 2022). The primary experimental method involves a

* Corresponding author.
E-mail address: frankcrespilho@iqsc.usp.br (F.N. Crespilho).

https://doi.org/10.1016/j.biosx.2024.100472
Received 2 February 2024; Received in revised form 15 March 2024; Accepted 19 March 2024
Available online 30 March 2024

clinical test based on reverse transcription–polymerase chain reaction (RT–PCR) assay, which enables sensitive and selective detection of viral nucleic acids (Tsang et al., 2021). However, RT–PCR assays are relatively expensive and require specialized personnel. Amid the pandemic, new detection methods for SARS-CoV-2 have emerged, such as liquid field-effect transistors (Seo et al., 2020) and electrochemical biosensors (Chaibun et al., 2021). Electrochemical biosensors, which utilize antigen–antibody interactions as analytes, have been recently reviewed (Mao et al., 2022). Nevertheless, numerous experimental challenges remain for electrochemical biosensors in detecting SARS-CoV-2, including portability, ease of operation, and high sensitivity. These factors are crucial for early detection of viral infections and for conducting reliable and efficient clinical trials.

The development of miniaturized architectures and the ability to modulate the chemistry interface are crucial for advancing next-generation molecular diagnostics. Here, we introduce a novel strategy for detecting SARS-CoV-2 in human saliva by functionalizing miniaturized flexible carbon fiber (FCF)-based electrodes with specific antibodies against the virus. The clinical course of SARS-CoV-2 infection in humans comprises an acute phase followed by a convalescent phase of viral infection (Carvalho et al., 2021). Viral RNA in clinical samples, such as human saliva, is detectable during both the acute and mild phases and serves as a satisfactory diagnostic marker for COVID-19 infection (Teo et al., 2021). Serologic biomarkers, including immunoglobulin G (IgG) antibodies, are present in saliva and associated with the convalescent phase of infection (Robbiani et al., 2020). The human body produces immunoglobulin M (IgM), immunoglobulin A (IgA), and IgG antibodies during the seroconversion process, typically occurring within the first few days of SARS-CoV-2 infection (Lou et al., 2020). Furthermore, the presence of such antibodies in human body is correlated with disease severity and the extent of infection and in the context of the usability of flexible carbon fibers applied to biosensors and bioelectronics (Iost and Crespilho, 2012a) that we envisioned a new miniaturized sensor as an ultrasensitive platform for detection of SARS-CoV-2. Our study demonstrates, for the first time, that FCF-modified IgG electrodes serve as an ultrasensitive platform for detecting SARS-CoV-2 during both the acute and convalescent phases of infection.

2. Materials and methods

The reagents, apparatus, electrochemical experiments, and physicochemical characterizations are presented in the supporting information.

2.1. Preparation of FCF-based electrodes for SARS-CoV-2 detection

Fig. 1 shows the object of study of the biosensor (Fig. 1A), biosensor components (Fig. 1B) and the scheme of device preparation (Fig. 1C). Briefly, FCFs were cleaned in ultrasound bath for 5 min with a mixture of isopropyl alcohol and ultrapure water. After the cleaning process, FCF electrodes with area equal to 0.0511 cm^2 (Fig. 1D) were electrochemically activated in basic aqueous solution using chronoamperometry, washed in ultrapure water, dry under vacuum and mechanically miniaturized and placed in the 3D-printed electrochemical device. The preparation of the FCF devices was followed by the chemical modification of the surface with glutaraldehyde aqueous solution 5% (GLU) as a cross-linking agent by drop-casting (optimized GLU concentration, see Fig. S1). The electrodes were then storage at ~7 °C for 1 h before incubation with IgG previously mixed with SARS-CoV-2 phosphate buffer solution 0.1 mol L^{-1} pH 7.2 (IgG-SARS-CoV-2) (optimized IgG-SARS-CoV-2 concentration, Fig. S2); the chemical reaction was carried out overnight. Finally, bovine serum albumin (BSA) and Nafion solution (1%) (optimized Nafion® concentration, Fig. S3) was drop on to the surface of the FCF electrodes and dry under vacuum for 30 min before the electrochemical experiments (Fig. S4).

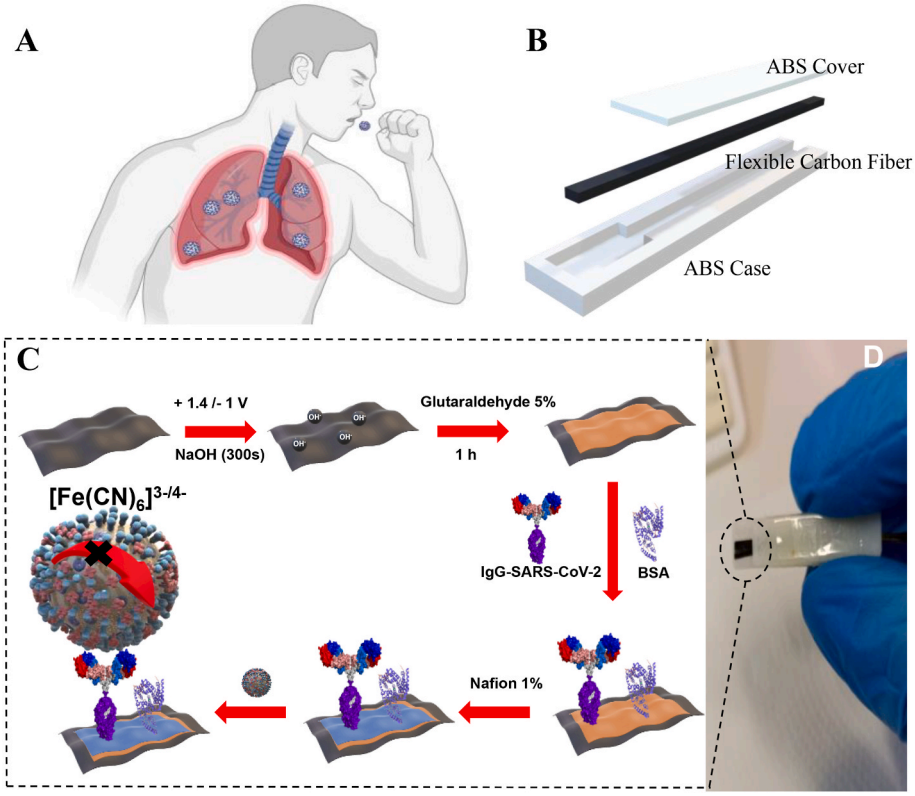

Fig. 1. Miniaturized and flexible bioelectronics for the detection of SARS-CoV-2. A) Biosensor target analyte. **B)** Biosensor components. **C)** Procedure for modifying FCFs for anchoring the IgG-SARS-CoV-2 antibodies and the detection of SARS-CoV-2. **D)** Photograph of the miniaturized FCF-based biosensor.

The evaluation of the limit of detection (LOD) of the FCF biosensor were obtained considering the standard deviation (SD) of the lowest concentration sample used in the experiments. The calibration curves were obtained using the reactivity index (RI) given by equation (1). With Ip_0 being the initial current and Ip being the final current after the interaction of the biosensor with the analyte.

$$R.I = \frac{I_{p_0} - I_p}{I_{p_0}} \quad (1)$$

3. Results and discussions

3.1. FCF-based biosensor

FCFs are promising materials for their applications in bioelectronics (Pereira et al., 2016). Their good conductivity and the possibility to modulate surface chemistry for biosensing are important characteristics that we highlight here to detect SARS-CoV-2. It was previously reported that the chemical (Martins et al., 2014) or electrochemical (Huang et al., 2010) treatment of FCFs improves the electrochemical response of bioelectrodes. FCFs were treated electrochemically in a basic medium to obtain quinone, hydroquinone, ketone, hydroxyl, and other compounds on the surface to improve the electrochemical response of electrodes (Pereira et al., 2017). The application of the anodic potential induces structural defects on the FCF surface increasing the density of edge-like carbon structures. Fig. 2 shows the electrochemical characterization and surface modification of the FCF.

Fig. 2A shows the cyclic voltammetry (CV) response of FCFs before (black) and after (red) electrochemical anodization in basic media. Electrochemistry was performed in 0.1 mol L^{-1} KCl in the presence of the redox probe [$Fe(CN)_6^{3-/4-}$] at a scan rate of 50 mV s^{-1}. The voltammetric profile of $Fe(CN)_6^{3-/4-}$ in the forward scan oxidizes Fe(II) ions to Fe(III) at E_{red} = +0.256 V vs. Ag/AgCl subsequently reducing Fe(III) back to Fe(II) in the reverse scan at E_{ox} = +0.275 V (Frenzel et al., 2017). The linear dependence of peak current densities (J/μA cm^{-2}) and the potential on the scan rate (mV s^{-1}) of the activated FCF post-treatment is shown in Fig. S5. The shift in the redox potential toward more positive or negative values upon increasing the scan rate is characteristic of a diffusion-controlled electrochemical process (Bard et al., 2022). The electrochemical process is also influenced by the adsorption of redox probes on the surface causing a current–potential shift upon increasing the scan rate. The slope is in accordance with the theoretical value of 0.059 V/pH at 25 °C for a one-electron reversible electron transfer reaction (Bard et al., 2022) (Fig. S5). Fig. 2B shows the long-term stability of the redox probe $Fe(CN)_6^{3-/4-}$ for activated FCFs after 50 cycles, the figure shows that there was no significant change in the current values nor a change in the oxidation and reduction potentials of the probe used, which indicates that the fibers present electrochemical stability, a good property for anchoring biomolecules for application in biosensing.

EIS was performed to characterize the ionic accessibility of pores on the surface of the Post-treatment FCF. EIS spectra were adjusted according to the equivalent circuit model (Orazem and Tribollet, n.d.) (Fig. S6). Fig. 2C displays the Nyquist plots of Post-treatment FCF (red), FCF-modified with adsorbed glutaraldehyde (FCF–GLU) (green), FCF-IgGS (Blue), and biosensor + RBD (pink) in which a spike appears for the low-frequency region used in the experiments. The charge transport resistance (R_{CT}) was first evaluated for each surface modification of Post-treatment FCF, FCF–GLU, FCF–IgGS, and the biosensor, increasing R_{CT} values to 75.25 kΩ, 89.9 kΩ, 140.7 kΩ and 164 kΩ (Table S1), respectively. This increase in R_{CT} values indicates a significantly slow diffusion process. In agreement with the Nyquist data, Fig. 2D shows the goat plots for each modification, where a change in maximum frequencies is observed as a function of each modification.

Fig. 2E shows the cyclic voltammogram for each modification step (FCF pristine) (black), Post-treatment FCF (red), FCF–GLU (green), FCF–IgGS (blue), FCF-IgGS/BSA (pink) and biosensor + RBD (cyan)),

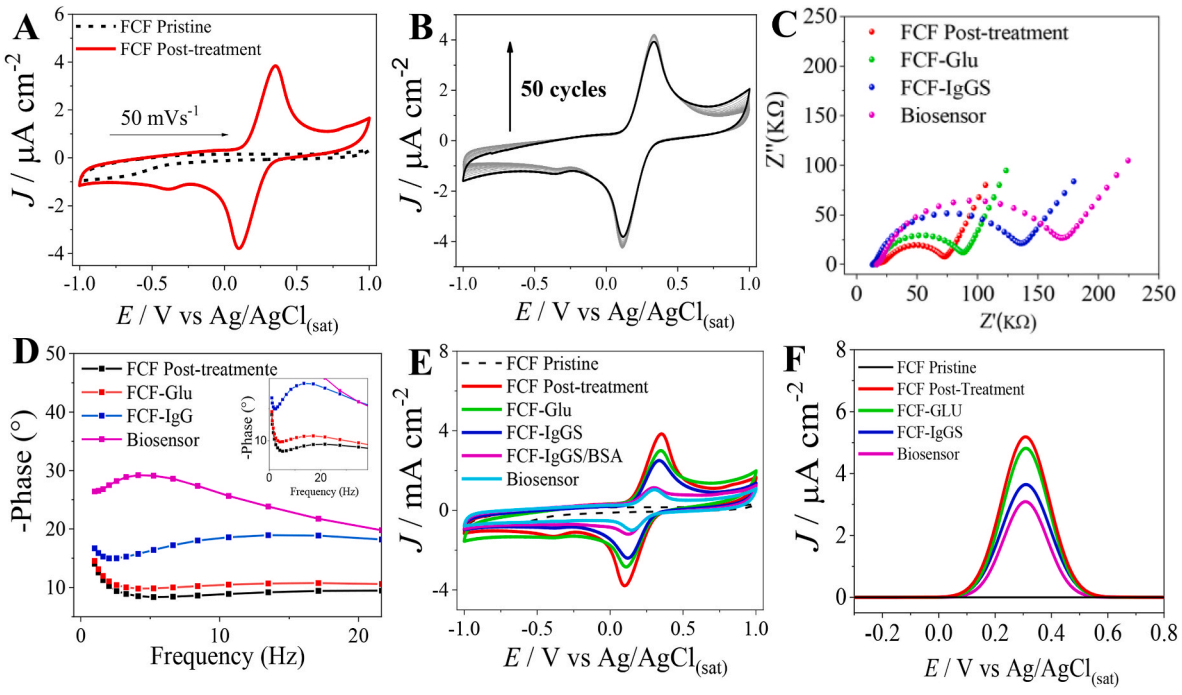

Fig. 2. Electrochemistry of FCF-based biosensor. A) Cyclic voltammograms of FCF pristine before (black) and after (red) anodization/oxidation in the basic medium. **B)** Voltammograms of preanodized FCF during 50 voltammetric cycles. **C)** Nyquist plots of different modifications: Post-treatment FCF (red), FCF–GLU (green), FCF–IgGS (blue), and biosensor + RBD (pink). **D)** Bode plots of different modifications: Post-treated FCF (black), FCF–GLU (red), FCF–IgGS (blue), and biosensor + RBD (pink). **E)** Cyclic voltammograms for different electrode configurations: FCF pristine (black), Post-treated FCF (red), FCF–GLU (green), FCF–IgGS (blue), FCF-IgGS/BSA (pink), and biosensor + RBD (cyan). **F)** Cyclic voltammograms for different electrode configurations: FCF pristine (black), Post-treatment FCF (red), FCF–GLU (green), FCF–IgGS (blue), and biosensor + RBD (pink). Supporting electrolyte KCl 0.1 mol L^{-1} and $Fe(CN)_6^{3-/4-}$ (0.5 mmol L^{-1}).

with the graphs it is possible to see the presence of the characteristic pairs of the electrochemical probe used. In addition, it is also possible to observe a shift in the oxidation potentials towards more negative regions while the reduction possibilities shifted towards more positive regions, which indicates an improvement in the system reversibility.

Fig. 2F shows the differential pulse voltammetry (DPV) graphs of each electrode configuration. FCF-GLU (green) does not influence the DPV response as compared to the Post-treatment FCF (red). A difference in DPV response is observed for FCF–IgGS with a significant shift in the current density upon modification of FCF with IgGS of approximately 27% and a further detection of RBD (pink) agrees with the EIS spectra in Fig. 2C. Moreover, the oxidation peak in the phosphate buffer as the supporting electrolyte related to the hexaferrocyanide redox probe can be observed at $E_{ox} = +0.30$ V vs. Ag/AgCl and shifts to $E_{ox} = +0.31$ V upon the addition of RBD to the supporting electrolyte. This suggests that RBD is adsorbed on the electrode surface. Fig. 3 shows the spectroscopic and morphological characterization of electrodes.

The structural characteristics of FCFs are similar to graphite but differ based on their structural organization. The layer planes of carbon atoms in turbostratic FCFs, such as those produced from the precursor polyacrylonitrile (PAN), are stacked randomly. Therefore, it is an important material in electrochemistry owing to its chemical and physical stability, in addition to the possibility of modulating its interfacial properties for application in biosensors and bioelectronics (Iost and Crespilho, 2012b). Initially, we compared microFTIR spectra of the pristine FCF (black), post-treated FCF (blue) and FCF-IgGS (blue) (Fig. 3A). The chemical structure of pristine FCF (black) shows the characteristic infrared peaks (Biniak et al., 1997): 2221 cm^{-1} (C≡N stretching) (Elagib et al., 2020), 1544 cm^{-1} and 1245 cm^{-1} (C=N stretching), 1095 cm^{-1} (C–CN stretching), 1288 cm^{-1} (C–O stretching group), 1627 cm^{-1} (C=O stretching group), and 1438 cm^{-1} and the peaks around 2923 cm^{-1} of –CH bending vibrations are related to $–CH_2/CH_3$ stretching modes. The post-treated FCF (red) shows the same functional chemical groups and the most prominent peaks related to carboxylic anhydrides at approximately 1823 cm^{-1} (Biniak et al., 1997). The presence of IgGS on the surface also resulted in significant changes in microFTIR spectra (blue). The molecular structure of biomolecules changes when placed on the surface, (Buijs et al., 1996; Giacomelli et al., 1999) as was also reported when IgGS was attached to the surface of the Post-treated FCF. The FTIR spectra of the FCF–IgGS electrode (blue) shows amide I, amide II, and amide III stretching bands at approximately 1689 cm^{-1}, 1585 cm^{-1}, and 1296 cm^{-1} (Carolina et al., 123AD), respectively. The presence of stretching modes is related to C=C at 2156 cm^{-1}, and the fingerprint infrared region is related to the SH group stretching band at approximately 2405 cm^{-1} (Cherepanov et al., 2022). Raman spectra were also recorded to obtain more structural information on the functionalization of FCFs.

Both chemical and electrochemical methods are used to induce exfoliation concomitantly with the generation of chemical functional groups on the surface of carbon materials. The anodic electrochemical oxidation of FCFs was responsible for the disorder induced by fibers. Fig. 3B shows the Raman spectra of the pristine FCF (black), Post-treated FCF (red), and FCF-IgGS electrode (blue). In the Raman spectrum, G-(1600 cm^{-1}) and D-band (1370 cm^{-1}) are the main signature bands of FCFs. The G-band is the signature of the sp^2 carbon network and is more prominent than the D-band in Raman spectra which represents the defects or disorder of the hexagonal carbon network (Ferrari, 2007). The D-band increases proportionally with the amount of disorder induced by the preanodic exfoliation procedure used in the present case for FCFs. The normalization of the relative intensity I_D/I_G ratio was used to estimate the disorder induced by FCFs (Pimenta et al., 2007). In the present study, the I_D/I_G ratios for the FCF, Post-treated FCF, and FCF-IgG are 0.71, 0.78, and 0.87 (Table S2), respectively. Additionally, FCF-IgGS shows a weak intensity band for the amino acid (tyrosine) at approximately 871 cm^{-1} (*) (Ota et al., 2016; Sato et al., 2022). Previous results show that Post-treated FCF induces more defective structures on FCFs prior to the immobilization of FCF-IgG.

Fig. 3C shows the changes in roughness and kurtosis of the three electrodes. We selected FCF with IgG-SARS-CoV-2 for further evaluation of the biosensor performance. Fig. 3D–F shows the atomic force microscopy (AFM) images of the FCF, Post-treated FCF, and FCF-IgGS, respectively. We evaluated the roughness and kurtosis of all electrodes. The FCF has a relatively smooth surface in comparison to the Post-treated FCF, which has increased surface defects owing to the presence of protuberances at the microscale level, in agreement with the Raman dataset. The roughness of Post-treated FCF marginally reduces from 2.8 nm to 2.0 nm, and the kurtosis significantly reduces from 6.7 to 4.1. The surface morphology of electrodes changes substantially with the modification of FCFs with IgG depicting protuberances with globular structures over the surface. Thus, the roughness increases to 4.8 nm, and the kurtosis further decreases to 3.2 for the FCF-IgG. In addition to AFM, SEM analyzes were also performed (Fig. S7). In the SEM images as well as in the AFM images, it is possible to clearly observe the morphology of the fibers, as well as the modification of the surface with each treatment.

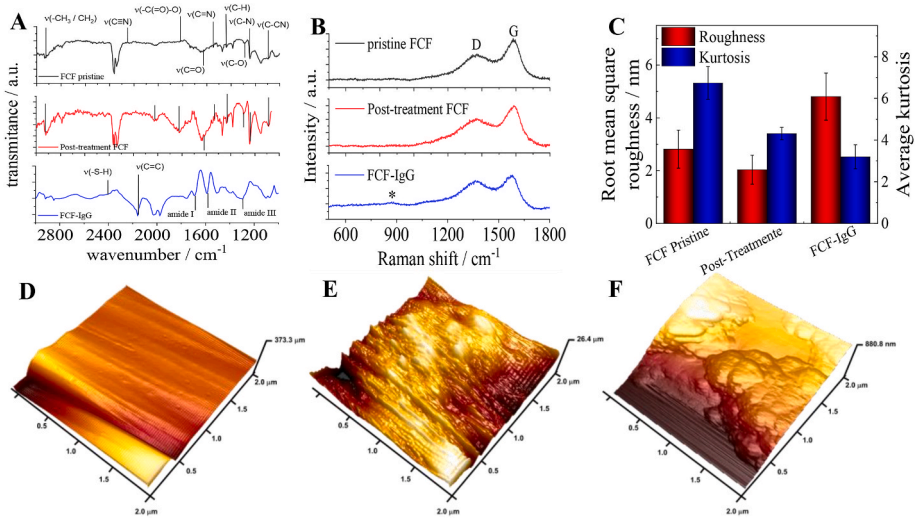

Fig. 3. Vibrational spectroscopic and morphological characterization of FCF-based biosensor. A) MicroFTIR spectrum of pristine FCF (black), Post-treatment FCF (red), and FCF–IgGS (blue). **B)** Raman spectrum of pristine FCF (black), Post-treatment FCF (red), and FCF–IgGS (blue). **C)** Relative evolution of roughness and kurtosis of pristine FCF, Post-treatment FCF, and FCF–IgGS electrodes. AFM images of **D)** pristine FCF, **E)** Post-treated FCF, and **F)** FCF-IgGS.

In the treatment of the fiber in a basic medium, the exfoliation of the fibers, the modification with glutaraldehyde wraps the fiber in a film and the anchoring of the antibody is evidenced by the appearance of architectures without defined morphology. These results together with the other results presented show that the fiber modification was effective.

3.2. Biosensor performance under standard conditions

The effect of RBD concentration on DPV signals recorded using the immunosensor was investigated using the biosensor for assay validation and the feasibility assessment of SARS-CoV-2 tests. A standard validation test was conducted. The method consists of detecting RBD (a portion of the spike protein) under standard experimental conditions (phosphate buffer solution 0.1 mol L^{-1}, pH 7.2). For more details, see the support information. Fig. 4 shows a schematic illustration of the interaction of the biosensor with RBD (Fig. 4A) and DPV voltammograms for the detection of RBD. Fig. 4B shows the DPV voltammograms for RBD detection indicating the electrochemical behavior of the biosensor before (black) and after interaction (red) with RBD. There is a progressive decrease in the current density when we increased the concentration of RBD in the supporting electrolyte solution (Fig. 4C). The oxidation peak of the hexaferrocyanide redox probe is observed at E_{ox} = +0.30 V vs. Ag/AgCl. The electrochemical behavior is attributed to the interaction between RBD with IgG-SARS-CoV-2 on the electrode surface to form an immunocomplex (Beduk et al., 2021). The formation of the immunocomplex affects current density owing to the blockage of the surface which hinders electron transport between $Fe(CN)_6^{3-/4-}$ and the fiber surface (Adeel et al., 2022b).

Fig. 4C shows the electrode performance at different RBD concentrations ranging from 1 ng mL^{-1} to 10 μg mL^{-1}. The RI increases with the increasing of the RBD concentration according to Equation (1). Moreover, a linear correlation is observed between the RI and the logarithm of RBD concentration (Fig. 4D) (RI *vs.* log [RBD]). The LOD is estimated to be 0.16 ± 0.0017 pg mL^{-1} based on the standard deviation of 10 consecutive blank analyses (95% confidence value, n = 3), and the value is within the range of values found in the literature. The high sensitivity may be due to carbon fibers with a high electrochemically active area and selectivity for IgG-SARS-CoV-2 (Kumar et al., 2023; Liang et al., 2022). Adeel and coworkers (Adeel et al., 2022a) reported a similar strategy for the detection of SARS-CoV-2 using carbon fibers coated with gold with a LOD of 0.11 ng mL^{-1}. Table S3 shows the comparison of the biosensor presented in this work and other works found in the literature for detection of SARS-CoV-2, where it is possible

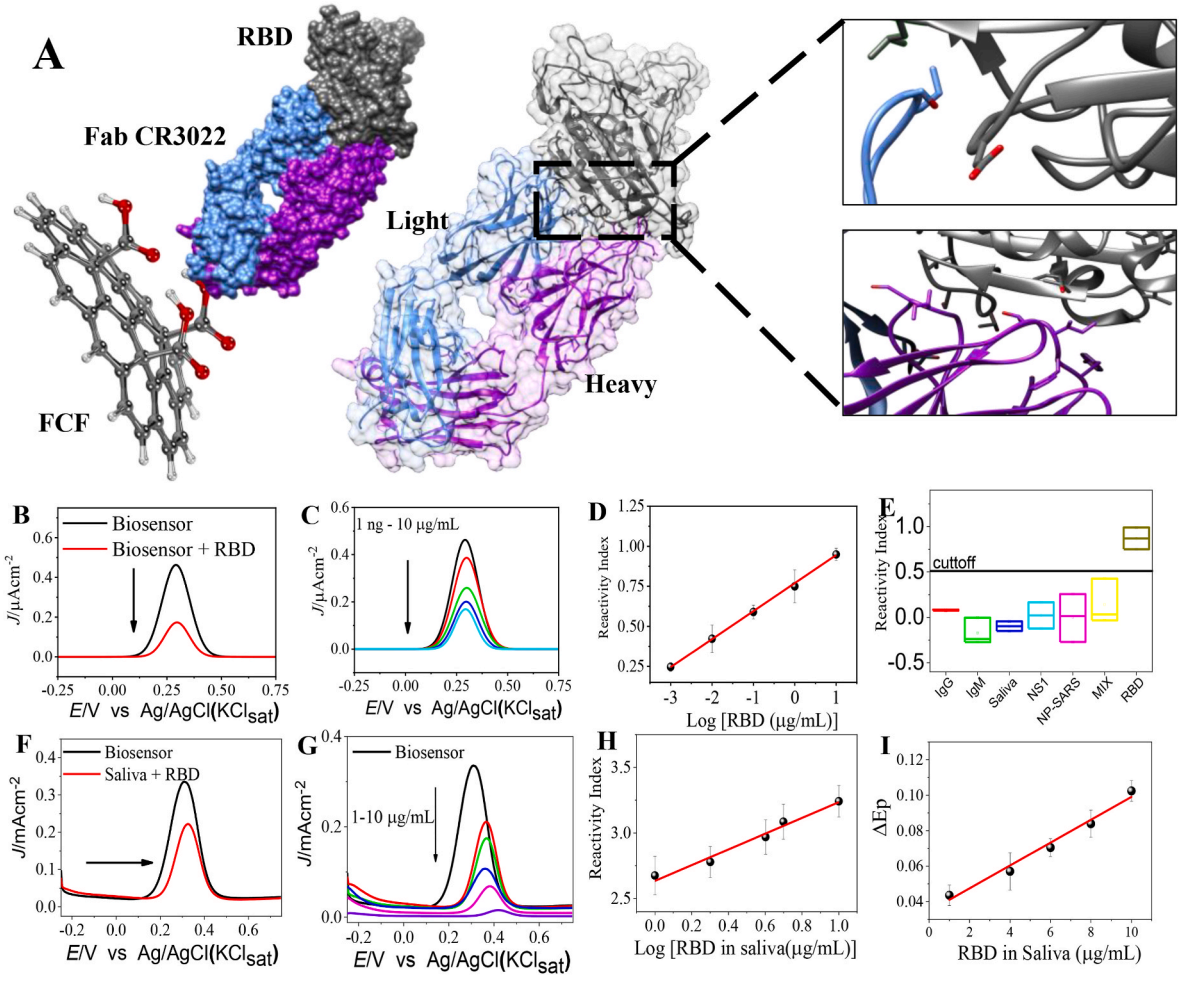

Fig. 4. Biosensor Performance. A) Illustrative scheme of the interaction of the biosensor (FCF-IgG-SARS-CoV-2) with the analyte (RBD). **B)** DPV voltammograms for biosensor (black) and Biosensor + RBD (red). **C)** DPV voltammograms of the biosensor in different concentrations of RBD (0.001–10 mg mL^{-1}). **D)** Calibration curve of the reactivity index *vs.* log[RBD/mg mL^{-1}]. **E)** Cross-reactivity assays of biosensor + IgG (Human) (red), biosensor + IgM (Humano) (green), biosensor + saliva (blue), biosensor + Dengue NPS1 (cyan) and biosensor + IgG RBD (pink). Concentration: 1 μg mL^{-1}. **F)** DPV voltammograms for biosensor (black) and Biosensor + (Saliva + RBD) (red). **G)** DPV voltammograms of the biosensor in different concentrations of RBD in saliva sample (0.001–10 mg mL^{-1}). **H)** Calibration curve of the reactivity index *vs.* log[RBD/mg mL^{-1}]. **I)** Calibration curve of ΔEp *vs.* log[RBD/mg mL^{-1}]. Supporting electrolyte: KCl 0.1 mol $L^{-1}$and $Fe(CN)_6^{3-/4-}$(0.5 mmol L^{-1}).

to observe that the LOD we obtained is in the range reported in the literature, indicating that our biosensor also has the potential to detect SARS-CoV-2 using FCF.

Apart from the sensitivity and reproducibility of the biosensor, its selectivity was evaluated through a cross-reactivity study. Four negative controls human IgG, human IgM, NS1 protein–dengue, Nucleocapsid protein-SARS-CoV-2 and mixture of proteins (NS1 protein–dengue, Nucleocapsid protein-SARS-CoV-2) was evaluated using the biosensor (Fig. 4E). The cut-off value of the current density is approximately set from the LOD at a concentration of 1 μg mL^{-1}. This shows that no cross-reactivity is observed for human IgG, human IgM, saliva 10% (v/v), NPS1 protein–dengue, Nucleocapsid protein-SARS-CoV-2, and a mix of proteins (NPS1 protein–dengue, Nucleocapsid protein-SARS-CoV-2) at a concentration of 1 μg mL^{-1}. The presence of such species does not interact with the biosensor. Cross-reactivity is an important factor in analyses, particularly in human saliva. Previously reported data show that real samples can be very complex leading to false positive and negative signals; hence, it is important to evaluate other species (Sarode and Sarode, 2021). The complexity of the actual sample will be studied in detail in the future using samples from infected patients. The stability and reproducibility of the biosensor were also analyzed. The reproducibility of RBD detection with a relative standard deviation (RSD) is 6.2% (Fig. S8A). The stability of DPV detection was evaluated for 25 successive measurements (Fig. S8B). There are no significant changes in the RI (RSD = 9%) indicating that the biosensor is relatively robust and efficient for RBD detection, in addition to these studies, the reproducibility of the biosensor was also evaluated in the presence of saliva (Fig. S8C), which presented an RSD = 10.37 %, indicating that the proposed detection method is reproducible.

In addition to the study under standard conditions, the behavior of the biosensor was also evaluated in enriched saliva samples. Fig. 4F displays the DPVs for the detection of RBD in saliva. The figure shows the voltammograms for the biosensor (black) and the saliva + RBD (red). From the Fig. 4F, it is possible to observe an electrochemical behavior like that observed for detection under standard conditions, in which there is a decrease in the current due to the formation of the immune complex. In addition, it is also possible to observe a displacement of the peak potential to more positive regions, behavior attributed to the complexity of the saliva sample. Biosensor performance was also evaluated at different concentrations of RBD in saliva (Fig. 4G). The profile was also like that presented by the biosensor under standard conditions, however, the peak potential shift was more pronounced, indicating that increasing RBD concentration in saliva can cause a difference in the dynamics between saliva constituents.

As in the indoor study, the biosensor's reactivity index was also evaluated as a function of concentration (Fig. 4H). From the graph, it is possible to observe that the reactivity index increases as a function of the increase RBD concentration. This result is interesting, not only because is possible to identify the presence of RBD in saliva, but also is possible to quantify it. However, in the study on enriched saliva, the result more expressive was the sharp shift in potential values due to the increase in RBD concentration in saliva (Fig. 4G). Through these data it was possible to determine that the peak potential varies linearly with increasing RBD concentration (Fig. 4I). This may indicate a new way to detect and quantify the presence of SARS-CoV-2 in saliva. We did not find similar behavior in the literature; however, everything indicates that it is due to the complexity of saliva samples. Due to this complexity, several factors must be considered for the application of the biosensor in this sample matrix (Krishnaveni, 2021).

3.3. Real samples analysis

The performance of the FCF biosensor in real saliva samples was also evaluated. Saliva samples were collected from patients after negative or positive clinical trials of SARS-CoV-2. Fig. S9 shows a schematic diagram of the FCF biosensor operation for the detection of SARS-CoV-2 in human saliva samples positive/negative. A specific antibody anchored on the FCF surface interacts with the spike protein to form the immunocomplex IgG-SARS-CoV-2. The formation of the immunocomplex promotes a steric impediment that blocks the electrochemical response of $Fe(CN)_6^{3-/4-}$ on the FCF surface. Fig. 5A shows the DPV for biosensor in the presence of the buffer, the figure shows that without the presence of SARS-CoV-2 there is no significant change in the current. Fig. 5B shows the Biosensor in the presence of antibodies present in saliva (IgM, IgG specific and non-specific for covid), however, as in Fig. 5A, no significant change in current is observed, as the biosensor is only selective for the Spike protein present in the SARS-CoV-2. The Fig. 5C show de DPV for positive test for SARS-CoV-2. Fig. 5D shows the DPV of negative test for SARS-CoV-2. A contrast is observed between Fig. 5C and D, where the biosensor in the presence of a positive SARS-CoV-2 sample occurs a significant decrease in the biosensor current, indicating the interaction between the IgGS and the Spike protein of the virus, already in an increase negative sample (Fig. 5D) no significant variation is observed indicating the selectivity of the biosensor and the differentiation of positive and negative samples.

Fig. 5E shows the sample dilution studies, in which with an increase in the dilution factor there is a decrease in the reactivity index, indicating that the best use of the sample is in the natural way in which it is collected. Therefore, the present study was carried out without diluting the saliva sample. In addition to the dilution factor, the time of exposure to the virus is also important to evaluate the applicability of the biosensor at different stages of the disease. In this sense, Fig. 5F displays the correlation between the days of symptoms and the biosensor reactivity index. This shows that in the first days of symptoms it is possible to identify the presence of SARS-CoV-2. This makes this biosensor promising for use at point of care, as it can identify the presence of SARS-CoV-2 on different days of symptoms.

Fig. 5G shows the ROC curve for in natura sample analysis. With the curve it was possible to estimate the cut-off at 0.25, which indicates that above this value samples are considered positive and below negative. With this value it was possible to construct a graph of separation of negative and positive samples (Fig. 5H). According to this graph, it was observed that there was a good separation of positive and negative samples, presenting only one false negative (Fig. 5I). These data indicate that the biosensor has excellent performance in natural samples, which can be comparable in performance to traditional detection methods for the analysis of SARS-CoV-2.

In addition to previous experiments, the effect of inactivation on the biosensor performance was analyzed. Fig. 5J displays the ROC curve for the biosensor applied to an inactive saliva sample. Experimentally, the cut-off point can be estimated at 0.25, similar to those previously found. Fig. 5K presents the separation graph between positive and negative samples, with the estimated cut-off point. There may be a good separation between positive and negative samples, however some analyzes were within the error range of the experiment, indicating that there was one false negative and two false positives (Fig. 5L). This indicates that despite the sensitivity of the biosensor, samples that undergo heat treatment for inactivation lose the configuration of the proteins that compose the virus and thus lose the binding specificity with the biosensor. However, this result indicates that despite of a loss sensitivity, the biosensor is still promising for the analysis of SARS-CoV-2.

In addition to the present strategy using the biosensors, employing protocols from the Brazilian Society of Laboratory Medicine ("Home - Abramed," n.d.), the accuracy, sensitivity, and specificity were estimated at 93.30% (Table S5) for detection in saliva samples in natura and 86.60%, 92.30%, and 82.35% for inactive saliva samples (Table S6). The decrease in the performance of the biosensor can be attributed to changes in the matrix of the heat-treated saliva samples. Moreover, it has been proven that the present strategy is highly efficient and selective for the detection of SARS-CoV-2. A kappa statistical test was also performed to assess the agreement between our dataset and the data obtained by RT–PCR analysis. The kappa coefficient is 0.93 for saliva

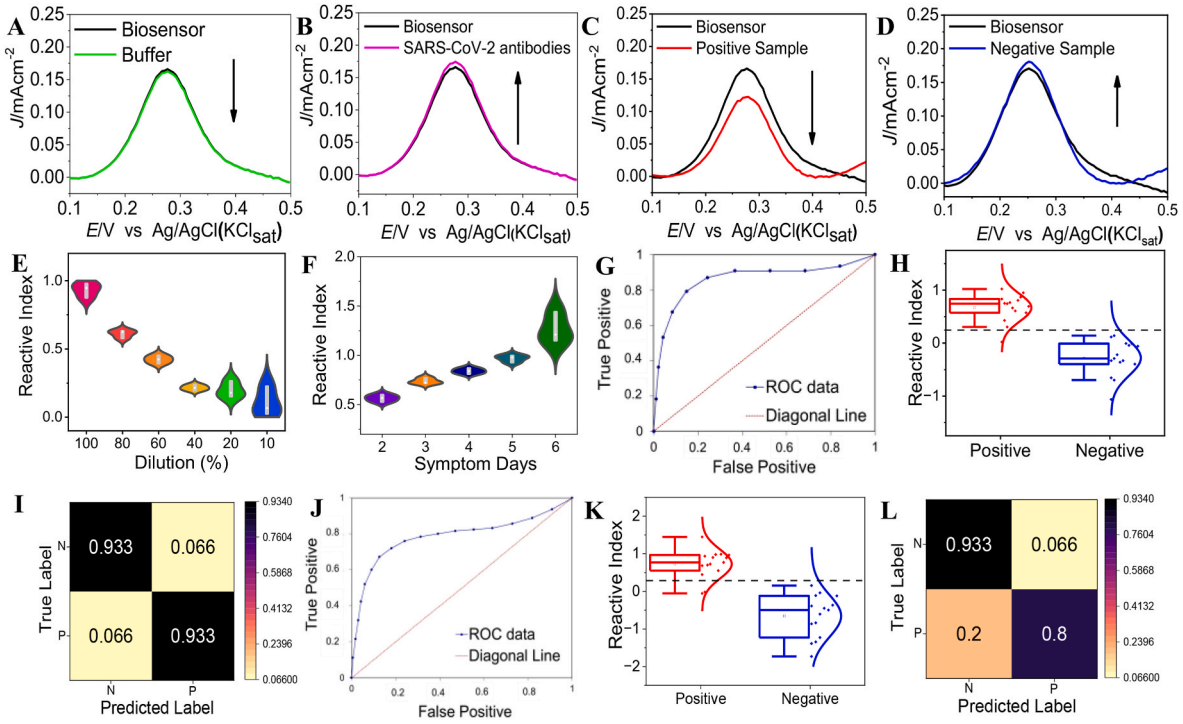

Fig. 5. FCF-based biosensor performance in human saliva samples. A) DPV of buffer (green) and biosensor (black). **B)** DPV of biosensor (black) and SARS-CoV-2 antibodies (pink). **C)** DPV of biosensor (black) positive samples for SARS-CoV-2 in saliva (red). **D)** DPV of biosensor (black) and negative samples for SARS-CoV-2 in saliva (blue). **E)** Study of dilution factor. **F)** Effect of days symptoms in reactive index. **G)** ROC curve of saliva samples in nature. **H)** The reactivity index of 10 saliva samples (5 positives and 5 negatives) are shown for saliva samples in nature. **I)** Confusion Matrix for saliva samples in nature. **J)** ROC curve of inactive samples. **K)** The reactivity index of 10 saliva samples (5 positives and 5 negatives) are shown for inactive saliva samples. **L)** Confusion Matrix for inactive sample. Supporting electrolyte: KCl 0.1 mol $L^{-1}$and $Fe(CN)_6^{3-/4-}$(0.5 mmol L^{-1}).

samples received from the patients agree with the data obtained from RT–PCR (Kraemer, 2015). In summary, the proposed miniaturized biosensor is label free, highly efficient, and selective for the detection of SARS-CoV-2 in human saliva. The estimated fabrication cost of the biosensor is approximately US$ 0.084, a considerably low price as compared to a few commercial diagnoses of COVID-19 (Table S7).

4. Conclusion

In this study, we present a straightforward and effective approach for designing biosensors based on FCF for the detection of SARS-CoV-2 in human saliva. The preanodized FCF in basic media offers a relatively large geometric surface area and exhibits good sensitivity towards electron transfer reactions for the redox probe pair [$Fe(CN)_6^{3-/4-}$]. Furthermore, by immobilizing IgG on the FCF-based biosensor, we enhanced its selectivity towards the spike protein RBD of SARS-CoV-2. To evaluate the biosensor's detection capability, we conducted experiments using RBD in phosphate buffer solution at pH 7.2, which provided optimal operating performance. The biosensor demonstrated a limit of detection of the order of 0.16 pg mL^{-1}, with an accuracy of 93.3% for analysis in real samples. Additionally, the results obtained with the biosensor showed a high K-index of 0.9 and exhibited a good correlation with RT-PCR analysis in saliva.

CRediT authorship contribution statement

Steffane Q. Nascimento: Writing – original draft, Formal analysis, Data curation, Conceptualization. **Rodrigo M. Iost:** Writing – original draft, Formal analysis, Data curation, Conceptualization. **Thiago C. Oliveira:** Writing – original draft, Formal analysis, Data curation, Conceptualization. **Rafael N. Colombo:** Writing – original draft, Formal analysis, Data curation, Conceptualization. **Luana C.I. Faria:** Formal analysis, Data curation, Conceptualization. **Thiago Bertaglia:** Formal analysis, Data curation, Conceptualization. **Jéssica C. Pacheco:** Formal analysis, Data curation, Conceptualization. **Mona N. Oliveira:** Validation, Methodology, Investigation, Formal analysis. **Erika R. Manuli:** Methodology, Investigation, Formal analysis, Data curation. **Geovana M. Pereira:** Formal analysis, Data curation, Conceptualization. **Ester C. Sabino:** Methodology, Investigation, Conceptualization. **Frank N. Crespilho:** Writing – original draft, Supervision, Resources, Project administration, Formal analysis, Data curation, Conceptualization.

Declaration of competing interest

The authors declare that they have no known competing financial interests or personal relationships that could have appeared to influence the work reported in this paper.

Data availability

The data that has been used is confidential.

Appendix A. Supplementary data

Supplementary data to this article can be found online at https://doi.org/10.1016/j.biosx.2024.100472.

References

Adeel, M., Asif, K., Alshabouna, F., Canzonieri, V., Rahman, M.M., Ansari, S.A., Güder, F., Rizzolio, F., Daniele, S., 2022a. Label-free electrochemical aptasensor for the detection of SARS-CoV-2 spike protein based on carbon cloth sputtered gold nanoparticles. Biosens. Bioelectron. X 12, 100256. https://doi.org/10.1016/J.BIOSX.2022.100256.

Adeel, M., Asif, K., Canzonieri, V., Barai, H.R., Rahman, M.M., Daniele, S., Rizzolio, F., 2022b. Controlled, partially exfoliated, self-supported functionalized flexible

graphitic carbon foil for ultrasensitive detection of SARS-CoV-2 spike protein. Sensor. Actuator. B Chem. 359, 131591 https://doi.org/10.1016/J.SNB.2022.131591.

Bard, A.J., Faulkner, L.R., White, H.S., 2022. Electrochemical Methods: Fundamental and Application 126.

Beduk, T., Beduk, D., de Oliveira Filho, J.I., Zihnioglu, F., Cicek, C., Sertoz, R., Arda, B., Goksel, T., Turhan, K., Salama, K.N., Timur, S., 2021. Rapid point-of-care COVID-19 diagnosis with a gold-nanoarchitecture-assisted laser-scribed graphene biosensor. Anal. Chem. 93, 8585–8594. https://doi.org/10.1021/ACS.ANALCHEM.1C01444/ASSET/IMAGES/LARGE/AC1C01444_0006.JPEG.

Behura, A., Naik, L., Patel, S., Das, M., Kumar, A., Mishra, A., Nayak, D.K., Manna, D., Mishra, A., Dhiman, R., 2023. Involvement of epigenetics in affecting host immunity during SARS-CoV-2 infection. Biochim Biophys Acta Mol Basis Dis 1869, 166634. https://doi.org/10.1016/J.BBADIS.2022.166634.

Biniak, S., Szymański, G., Siedlewski, J., Światkoski, A., 1997. The characterization of activated carbons with oxygen and nitrogen surface groups. Carbon N Y 35, 1799–1810. https://doi.org/10.1016/S0008-6223(97)00096-1.

Buijs, J., Norde, W., Lichtenbelt, J.W.T., 1996. Changes in the secondary structure of adsorbed IgG and F(ab')2 studied by FTIR spectroscopy. Langmuir 12, 1605–1613. https://doi.org/10.1021/LA950665S/ASSET/IMAGES/LARGE/LA950665SF00009.JPEG.

Seo, G., Lee, G., Kim, M.J., Baek, S.H., Choi, M., Ku, K.B., Lee, C.S., Jun, S., Park, D., Kim, H.G., Kim, S.J., 2020. Rapid Detection of COVID-19 Causative Virus (SARS-CoV-2) in Human Nasopharyngeal Swab Specimens Using Field-Effect Transistor-Based. Biosensor 14 (4), 5135–5142. https://doi.org/10.1021/acsnano.0c02823.

Teo, A.K.J., Choudhury, Y., Tan, I.B., Cher, C.Y., Chew, S.H., Wan, Z.Y., Cheng, L.T.E., Oon, L.L.E., Tan, M.H., Chan, K.S., Hsu, L.Y., 2021. Saliva is more sensitive than nasopharyngeal or nasal swabs for diagnosis of asymptomatic and mild COVID-19 infection. Sci. Rep. 11, 1–8. https://doi.org/10.1038/s41598-021-82787-z.

Tsang, N.N.Y., So, H.C., Ng, K.Y., Cowling, B.J., Leung, G.M., Ming, D.K., 2021. Diagnostic performance of different sampling approaches for SARS-CoV-2 RT-PCR testing: a systematic review and meta-analysis. Lancet Infect Dis 21, 1233–1245. https://doi.org/10.1016/S1473-3099(21)00146-8.

Wrapp, D., Wang, N., Corbett, K.S., Goldsmith, J.A., Hsieh, C.-L., Abiona, O., Graham, B. S., McLellan, J.S., 2020. Cryo-EM Structure of the 2019-nCoV Spike in the Prefusion Conformation. bioRxiv 367, 1260–1263. https://doi.org/10.1126/science.abb2507.

Zaki, A.M., Boheemen, S., Bestebroer, T.M., Osterhaus, A.D.M.E., Fouchier, R.A.M., 2012. Isolation of a Novel Coronavirus from a Man with Pneumonia in Saudi Arabia. N Engl J Med 367, 1814–1820. https://doi.org/10.1056/NEJMOA1211721/SUPPL_FILE/NEJMOA1211721_DISCLOSURES.PDF.

Carolina, C., Bandeira, S., Cristina, K., Madureira, R., Rossi, M.B., Gallo, J.F., Paula, A., Aguirra Da Silva, M., Lopes Torres, V., Alves De Lima, V., Júnior, N.K., Dias Almeida, J., Zerbinati, R.M., Braz-Silva, P.H., Angelo, J., Lindoso, L., Da, H., Martinho, S., 123AD. Micro-Fourier-transform infrared reflectance spectroscopy as tool for probing IgG glycosylation in COVID-19 patients. Sci. Rep. | 12, 4269.. https://doi.org/10.1038/s41598-022-08156-6.

Carvalho, T., Krammer, F., Iwasaki, A., 2021. The first 12 months of COVID-19: a timeline of immunological insights. Nat Rev Immunol 21, 245–256. https://doi.org/10.1038/s41577-021-00522-1.

Chaibun, T., Puenpa, J., Ngamdee, T., Boonapatcharoen, N., Athamanolap, P., O'Mullane, A.P., Vongpunsawad, S., Poovorawan, Y., Lee, S.Y., Lertanantawong, B., 2021. Rapid electrochemical detection of coronavirus SARS-CoV-2,12,, 1–10. https://doi.org/10.1038/s41467-021-21121-7.

Cherepanov, I., Sidorov, A., Terentiev, A., Menshikova, D., Beduleva, L., Menshikov, I., 2022. Fourier-transform infrared spectroscopy of human IgG Fc fragments, which are a promising drug for the treatment of autoimmune diseases. Spectrochim. Acta Mol. Biomol. Spectrosc. 278, 121299 https://doi.org/10.1016/J.SAA.2022.121299.

Robbiani, Davide F, Gaebler, Christian, Muecksch, Frauke, Lorenzi, Julio C C, Wang, Zijun, Cho, Alice, Agudelo, Marianna, Barnes, Christopher O, Gazumyan, Anna, Finkin, Shlomo, Hägglöf, Thomas, Oliveira, Thiago Y, Viant, Charlotte, Hurley, Arlene, Hoffmann, Hans-Heinrich, Millard, Katrina G, Kost, Rhonda G, Cipolla, Melissa, Gordon, Kristie, Bianchini, Filippo, Chen, Spencer T, Ramos, Victor, Patel, Roshni, Dizon, Juan, Shimeliovich, Irina, Mendoza, Pilar, Hartweger, Harald, Nogueira, Lilian, Pack, Maggi, Horowitz, Jill, Schmidt, Fabian, Weisblum, Yiska, Michailidis, Eleftherios, Ashbrook, Alison W, Waltari, Eric, Pak, John E, Huey-Tubman, Kathryn E, Koranda, Nicholas, Hoffman, Pauline R, West Jr, Anthony P, Rice, Charles M, Hatziioannou, Theodora, Bjorkman, Pamela J, Bieniasz, Paul D, Caskey, Marina, Nussenzweig, Michel C, 2020. Convergent antibody responses to SARS-CoV-2 in convalescent individuals 584, 437–442. https://doi.org/10.1038/s41586-020-2456-9.

Dhama, K., Nainu, F., Frediansyah, A., Yatoo, M.I., Mohapatra, R.K., Chakraborty, S., Zhou, H., Islam, M.R., Mamada, S.S., Kusuma, H.I., Rabaan, A.A., Alhumaid, S., Mutair, A.A., Iqhrammullah, M., Al-Tawfiq, J.A., Mohaini, M.A., Alsalman, A.J., Tuli, H.S., Chakraborty, C., Harapan, H., 2023. Global emerging Omicron variant of SARS-CoV-2: Impacts, challenges and strategies 16, 4–14.

Elagib, T.H.H., Hassan, E.A.M., Liu, B., Han, K., Yu, M., 2020. Evaluation of composite PAN fibers incorporated with carbon nanotubes and titania and their performance during the microwave-induced pre-oxidation. Carbon Lett. 30, 235–245. https://doi.org/10.1007/S42823-019-00092-2/FIGURES/6.

Ferrari, A.C., 2007. Raman spectroscopy of graphene and graphite: disorder, electron–phonon coupling, doping and nonadiabatic effects. Solid State Commun. 143, 47–57. https://doi.org/10.1016/J.SSC.2007.03.052.

Frenzel, N., Hartley, J., Frisch, G., 2017. Voltammetric and spectroscopic study of ferrocene and hexacyanoferrate and the suitability of their redox couples as internal standards in ionic liquids. Phys. Chem. Chem. Phys. 19, 28841–28852. https://doi.org/10.1039/C7CP05483A.

Giacomelli, C.E., Bremer, M.G.E.G., Norde, W., 1999. ATR-FTIR study of IgG adsorbed on different silica surfaces. J. Colloid Interface Sci. 220, 13–23. https://doi.org/10.1006/JCIS.1999.6479.

Hoffmann, Markus, Kleine-Weber, Hannah, Schroeder, Simon, Krüger, Nadine, Herrler, Tanja, Erichsen, Sandra, Schiergens, Tobias S., Herrler, Georg, Wu, Nai-Huei, Nitsche, Andreas, Müller, Marcel A., Drosten, Christian, Pöhlmann, Stefan, 2020. SARS-CoV-2 Cell Entry Depends on ACE2 and TMPRSS2 and Is Blocked by a Clinically Proven Protease Inhibitor 181, 271–280. https://doi.org/10.1016/j.cell.2020.02.052.

Home - Abramed [WWW Document], n.d. URL https://abramed.org.br/(accessed 1.26.23).

Goldsmith, C.S, Tatti, K.M., Ksiazek, T.G., Rollin, P.E., Comer, J.A., Lee, W.W., Rota, P. A., Bankamp, B., Bellini, W.J., Zaki, S.R., 2004. Ultrastructural Characterization of SARS Coronavirus 10, 320–326. https://doi.org/10.3201/eid1002.030913.

Gomari, M.M., Tarighi, P., Choupani, E., Abkhiz, S., Mohamadzadeh, M., Rostami, N., Sadroddiny, E., Baammi, S., Uversky, V.N., Dokholyan, N.V., 2023. Structural evolution of Delta lineage of SARS-CoV-2. Int. J. Biol. Macromol. 226, 1116–1140. https://doi.org/10.1016/J.IJBIOMAC.2022.11.227.

Gorbalenya, A.E., Baker, S.C., Baric, R.S., de Groot, R.J., Drosten, C., Gulyaeva, A.A., Haagmans, B.L., Lauber, C., Leontovich, A.M., Neuman, B.W., Penzar, D., Perlman, S., Poon, L.L.M., Samborskiy, D.V., Sidorov, I.A., Sola, I.S., Ziebuhr, J., 2020. The species Severe acute respiratory syndromerelated coronavirus: classifying 2019-nCoV and naming it SARS-CoV-2 5, 536–544. https://doi.org/10.1038/s41564-020-0695-z.

Huang, J., Liu, Y., You, T., 2010. Carbon nanofiber based electrochemical biosensors: a review. Anal. Methods 2, 202–211. https://doi.org/10.1039/B9AY00312F.

Iost, R.M., Crespilho, F.N., 2012a. Layer-by-layer self-assembly and electrochemistry: applications in biosensing and bioelectronics. Biosens. Bioelectron. 31, 1–10. https://doi.org/10.1016/J.BIOS.2011.10.040.

Iost, R.M., Crespilho, F.N., 2012b. Layer-by-layer self-assembly and electrochemistry: applications in biosensing and bioelectronics. Biosens. Bioelectron. 31, 1–10. https://doi.org/10.1016/J.BIOS.2011.10.040.

Kraemer, H.C., 2015. Kappa Coefficient. Wiley StatsRef: Statistics Reference Online, pp. 1–4. https://doi.org/10.1002/9781118445112.STAT00365.PUB2.

Krishnaveni, P., 2021. Electron transfer studies of a conventional redox probe in human sweat and saliva bio-mimicking conditions. Scientific Reports 11, 1–13. https://doi.org/10.1038/s41598-021-86866-z.

Kumar, T.H.V., Srinivasan, S., Krishnan, V., Vaidyanathan, R., Babu, K.A., Natarajan, S., Veerapandian, M., 2023. Peptide-based direct electrochemical detection of receptor binding domains of SARS-CoV-2 spike protein in pristine samples. Sensor. Actuator. B Chem. 377, 133052 https://doi.org/10.1016/J.SNB.2022.133052.

Liang, Q., Huang, Y., Wang, M., Kuang, D., Yang, Jiahua, Yi, Y., Shi, H., Li, J., Yang, Jie, Li, G., 2022. An electrochemical biosensor for SARS-CoV-2 detection via its papain-like cysteine protease and the protease inhibitor screening. Chem. Eng. J. 452, 139646. https://doi.org/10.1016/J.CEJ.2022.139646, 139646.

Lou, B., Li, T.D., Zheng, S.F., Su, Y.Y., Li, Z.Y., Liu, W., Yu, F., Ge, S.X., Zou, Q.D., Yuan, Q., Lin, S., 2020. Serology characteristics of SARS-CoV-2 infection after exposure and post-symptom onset. Eur. Respir. J. 56, 2000763. https://doi.org/10.1183/13993003.00763-2020.

Lu, R., Zhao, X., Li, J., Niu, P., Yang, B., Wu, H., Wang, W., Song, H., Huang, B., Zhu, N., Bi, Y., Ma, X., Zhan, F., Wang, L., Hu, T., Zhou, H., Hu, Z., Zhou, W., Zhao, L., Chen, J., Tan, W., 2020. The Lancet 395, 565–574. https://doi.org/10.1016/S0140-6736(20)30251-8.

Mao, S., Fu, L., Yin, C., Liu, X., 2022. The role of electrochemical biosensors in SARS-CoV-2 detection: a bibliometrics-based analysis. and review 12, 22592–22607. https://doi.org/10.1039/D2RA04162F.

Martins, M.V.A., Pereira, A.R., Luz, R.A.S., Iost, R.M., Crespilho, F.N., 2014. Evidence of short-range electron transfer of a redox enzyme on graphene oxide electrodes. Phys. Chem. Chem. Phys. 16, 17426–17436. https://doi.org/10.1039/C4CP00452C.

Orazem, M.E., Tribollet, B., n.d. Electrochemical Impedance Spectroscopy.

Ota, C., Noguchi, S., Nagatoishi, S., Tsumoto, K., 2016. Assessment of the protein-protein interactions in a highly concentrated antibody solution by using Raman spectroscopy. Pharm. Res. (N. Y.) 33, 956–969. https://doi.org/10.1007/S11095-015-1842-8/FIGURES/12.

Pereira, A.R., De Souza, J.C.P., Gonçalves, A.D., Pagnoncelli, K.C., Crespilho, F.N., 2017. Bioelectrooxidation of ethanol using NAD-dependent alcohol dehydrogenase on oxidized flexible carbon fiber arrays. J. Braz. Chem. Soc. 28, 1698–1707. https://doi.org/10.21577/0103-5053.20170012.

Pereira, A.R., de Souza, J.C.P., Iost, R.M., Sales, F.C.P.F., Crespilho, F.N., 2016. Application of carbon fibers to flexible enzyme electrodes. J. Electroanal. Chem. 780, 396–406. https://doi.org/10.1016/J.JELECHEM.2016.01.004.

Pimenta, M.A., Dresselhaus, G., Dresselhaus, M.S., Cançado, L.G., Jorio, A., Saito, R., 2007. Studying disorder in graphite-based systems by Raman spectroscopy. Phys. Chem. Chem. Phys. 9, 1276–1290. https://doi.org/10.1039/B613962K.

Ravi, N., Cortade, D.L., Ng, E., Wang, S.X., 2020. Diagnostics for SARS-CoV-2 detection: A comprehensive review of the FDA-EUA COVID-19 testing landscape. Biosens Bioelectron 165, 112454. https://doi.org/10.1016/j.bios.2020.112454.

Sarode, S.C., Sarode, G.S., 2021. Saliva sample and SARS-CoV-2 detection: more complexities than clarity. J. Oral Biol. Craniofac. Res. 11, 500–501. https://doi.org/10.1016/J.JOBCR.2021.07.002.

Sato, Y., Nagatoishi, S., Noguchi, S., Tsumoto, K., 2022. Raman spectroscopic analysis of highly-concentrated antibodies under the acid-treated conditions. https://doi.org/10.48550/arxiv.2207.06556.

Wiersinga, W.J., Rhodes, A, Cheng, A.C., Peacock, S.J., Prescott, H.C., 2020. Pathophysiology, Transmission, Diagnosis, and Treatment of Coronavirus Disease 2019 (COVID-19). JAMA 324, 782–793. https://doi.org/10.1001/jama.2020.12839.

Zhong, N.S., Zheng, B.J., Li, Y.M., Poon, L.L.M., Xie, Z.H., Chan, K.H., Li, P.H., Tan, S.Y., Chang, Q., Xie, J.P., Liu, X.Q., 2003. Epidemiology and cause of severe acute respiratory syndrome (SARS) in Guangdong, People's Republic of China, in February, 2003. Biosens Bioelectron. 362, 1353–1358. https://doi.org/10.1016/S0140-6736(03)14630-2.